2024 IEEE/RSJ International Conference on Intelligent Robots and Systems (IROS)
October 14-18, 2024. Abu Dhabi, UAE

Compliance Optimization Control for Rigid-Soft Hybrid System and its Application in Humanoid Robot Motion Control

Zewen He, Taiki Ishigaki, and Ko Yamamoto

***Abstract*— Flexibility and softness play a significant role in dynamic human motions. This includes the flexibility owing to ligaments in the human body and the softness of external structures such as a leaf-spring-type prosthesis. Thus, robotic systems need to utilize such flexibility to achieve dynamic and energy-efficient motion. In this study, we proposed a compliance optimization-based control framework for a rigid-soft hybrid robot system where the continuous deformation of a flexible structure is represented using the piece-wise constant strain (PCS) model. We divided the hybrid system into two states: single support and double support. We validated the proposed method in these states using forward dynamics simulations, assuming a hybrid link system that consists of a humanoid robot with a flexible prosthesis.**

I. Introduction

Tendons and ligaments provide internal flexibility in human hopping or running motions. However, this can also be provided by a leaf-spring-type prosthesis leg. These flexible elements are crucial in absorbing impact and storing energy during dynamic motions. A representative example is a Paralympic athlete wearing a sports-specific prosthesis leg. In robotics, and especially in humanoids, several attempts have been made to introduce flexible elements [1], [2].

Recently, several studies have focused on flexible structure modeling, indicating increased attention toward soft robotics research. While the finite element method can be used to model a complicated deformation, the continuous deformation of a rod or beam structure is modeled based on the Cosserat theory [3]. Some variations such as the piece-wise constant strain (PCS) model [4] discretizes a continuous deformation into several piece-wise segments. Ishigaki and Yamamoto [5] proposed a hybrid-link system comprising the PCS model and a floating-base multi-link system considering contact forces. They also presented a forward dynamics simulation by a humanoid robot with a flexible beam on its leg. However, they assumed that all joints were actively controllable, including passive flexibility. For motion control involving passive flexibility or compliance, model predictive control, and learning-based control [6] have been proposed. Moreover, some studies have focused on the stiffness- or passivity-based control of hybrid robots for robot manipulator applications [7], [8].

This study presents an approach to directly optimize the active joint viscoelasticity in the rigid parts to achieve task-space viscoelasticity despite the passive viscoelasticity. For a hybrid link system comprising a humanoid robot with leaf-spring-type prosthesis legs, we consider two types of motion states: the single and double support states. For the single support, we propose a compliance optimization framework that optimizes the active compliance matrix, including the coupling term between the active and passive joints. While this method is based on a static compliance relationship, we propose the other method for the double support state based on the dynamically consistent compliance relationship [9]. The proposed methods for standing balance and vertical hopping control are validated through forward dynamics simulation. The rest of this paper is organized as follows. In Section II, we introduce the problem setting, including the PCS model and hybrid link system (Fig. 1(a)). Then, the compliance optimization methods in the single and double support states are proposed in Sections III and IV, respectively. In Section V, we present the simulation results and provide discussions. Finally, the obtained results are summarized in Section VI. In the rest of the paper, we use the following notations:

- $\boldsymbol{O}$ and $\boldsymbol{E}$ denote the zero and unit matrices;
- $*_{\mathrm{ref}}$ denotes the reference value of a quantity $*$;
- $\Delta * = *_{\mathrm{ref}} - *$ denotes the error between an arbitrary quantity $*$ and its reference value;
- $\boldsymbol{X}^\sharp$ denotes the pseudo-inverse of $\boldsymbol{X}$. When $\boldsymbol{X}$ is horizontally-long and full row rank, $\boldsymbol{X}^\sharp = \boldsymbol{X}^T(\boldsymbol{X}\boldsymbol{X}^T)^{-1}$; when $\boldsymbol{X}$ is vertically-long and full column rank, $\boldsymbol{X}^\sharp = (\boldsymbol{X}^T\boldsymbol{X})^{-1}\boldsymbol{X}^T$;
- For optimization problem:

$$\min_{\boldsymbol{X}} \ \frac{1}{2}\|\boldsymbol{X}_{\mathrm{ref}} - \boldsymbol{X}\|^2 \quad \text{s.t. } \boldsymbol{A}\boldsymbol{X}\boldsymbol{B} = \boldsymbol{C} \qquad (1)$$

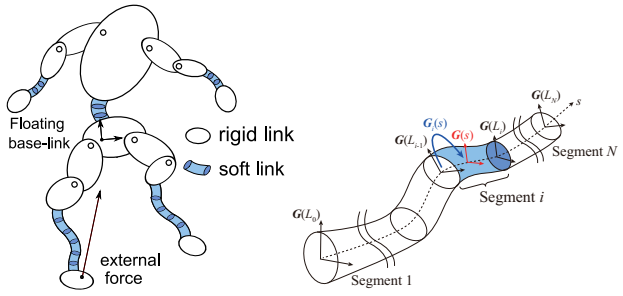

Fig. 1. (a) Illustration of a hybrid multi-link system. (b) Schematic illustration of the PCS model [4]. A beam or rod structure is divided into a finite number of *segments*. It is assumed that in each segment the six-dimensional strain is spatially constant (while in this study we only consider 3 angular strains).

This research is supported by JSPS KAKENHI Grant Number 21H01282.
The authors are with the Department of Mechano-informatics, Univ. of Tokyo, 7-3-1 Hongo, Bunkyo-ku, Tokyo 113-8656, Japan. he-zewen@ynl.t.u-tokyo.ac.jp

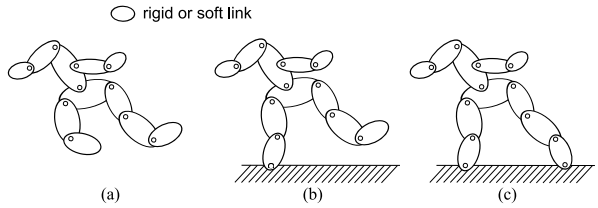

Fig. 2. (a) Floating-base system; (b) open kinematic chain with a fixed link representing the single support state; and (c) closed kinematic chain representing the double support state.

the analytical general solution is

$$\boldsymbol{X} = \boldsymbol{A}^{\sharp}\boldsymbol{C}\boldsymbol{B}^{\sharp} + \boldsymbol{X}_{\mathrm{ref}} - \boldsymbol{A}^{\sharp}\boldsymbol{A}\boldsymbol{X}_{\mathrm{ref}}\boldsymbol{B}\boldsymbol{B}^{\sharp}. \quad (2)$$

II. Problem Setting

A. Hybrid Multi-link System [5]

Ishigaki and Yamamoto [5] proposed a hybrid-link system integrating a rigid-body multi-link system and flexible structure. In particular, the latter is approximated using the PCS model. Let $\boldsymbol{H}(s) \in \mathrm{SE}(3)$ be the configuration curve of a continuously deformable beam or rod structure where s denotes the center axis coordinate. The six-dimensional *strain* $\boldsymbol{\xi}(s)$ at s is defined as

$$[\boldsymbol{\xi}(s)\times] := \boldsymbol{H}^{-1}(s)\frac{\partial \boldsymbol{H}(s)}{\partial s} \in \mathfrak{se}(3) \quad (3)$$

where $[*\times]$ represents a vector cross-product operation. In the PCS model, the structure is divided into a finite number of *segments*, and the strain is assumed to be constant $\boldsymbol{\xi}_i \in \mathbb{R}^6$ in each segment i. Combining $\boldsymbol{\xi}_i$ for all segments, the generalized coordinate of the PCS model is defined as $\boldsymbol{\theta}_S = \begin{bmatrix}\boldsymbol{\xi}_1^T & \cdots & \boldsymbol{\xi}_{N_S}^T\end{bmatrix}^T$ where N_S is the number of segments. The schematic illustration of the PCS model is shown in Fig. 1(b). The kinematics and dynamic formula structures of the PCS model are similar to those of a rigid-body multi-link system, which allows us to easily integrate those two models. We call this model a *hybrid* model in that the rigid and soft structure are integrated, and also because the PCS model deals with a *continuous* deformation despite its piecewise assumption. In contrast, the rigid-link model deals with a *discrete* deformation due to a mechanical pair.

Assuming that the base-link is not fixed to the environment as shown in Fig. 2(a), let $\boldsymbol{H}_0 \in \mathrm{SE}(3)$ and $\boldsymbol{\eta}_0 \in \mathbb{R}^6$ denote the homogeneous transformation matrix and velocity twist vector of the base-link, respectively. The generalized coordinates of the hybrid system and its velocity can be defined by: $\boldsymbol{q} := \{\boldsymbol{H}_0,\ \begin{bmatrix}\boldsymbol{\theta}_R^T & \boldsymbol{\theta}_S^T\end{bmatrix}^T\}$, $\dot{\boldsymbol{q}} := \begin{bmatrix}\boldsymbol{\eta}_0^T & \dot{\boldsymbol{\theta}}_R^T & \dot{\boldsymbol{\theta}}_S^T\end{bmatrix}^T$, where $\boldsymbol{\theta}_R$ are the generalized coordinates of the rigid part. The dynamics of the hybrid link system can be represented as

$$\mathcal{M}(\boldsymbol{q})\ddot{\boldsymbol{q}} + \boldsymbol{\beta} = \begin{bmatrix}\boldsymbol{0}^T & \boldsymbol{\tau}_R^T & \boldsymbol{\tau}_S^T\end{bmatrix}^T + \mathcal{J}_C^T\boldsymbol{f}_C \quad (4)$$

where $\mathcal{M}(\boldsymbol{q})$ is the total inertia matrix; $\boldsymbol{\beta}(\boldsymbol{q}, \dot{\boldsymbol{q}})$ is the bias vector; and $\boldsymbol{\tau}_i$ is the generalized force vector, with the indexes 0 for the base-link, R for the rigid-link part, and S for the PCS model part. Note that the soft part can be located at any position in the hybrid system, not necessarily limited to the end. Also, $\boldsymbol{f}_C := \begin{bmatrix}\boldsymbol{f}_{C,1}^T & \cdots & \boldsymbol{f}_{C,N_C}^T\end{bmatrix}^T \in \mathbb{R}^{3N_C}$ is the sum of external contact force (N_C is the number of contact points), whereas $\mathcal{J}_C^T := \begin{bmatrix}\mathcal{J}_{C,1}^T & \cdots & \mathcal{J}_{C,N_C}^T\end{bmatrix} \in \mathbb{R}^{(6+N_R+3N_S)\times 3N_C}$ (N_R is the rigid-part DoFs, and $3N_S$ means that we only consider 3 angular strain for each soft segment) is the Jacobian matrix at the corresponding contact point. In the case of a humanoid system, for example, $\boldsymbol{f}_C$ includes the ground reaction force. For a passive soft robot, $\boldsymbol{\tau}_S$ is represented using stiffness and viscosity as:

$$\boldsymbol{\tau}_S = \boldsymbol{K}_S\Delta\boldsymbol{\theta}_S - \boldsymbol{D}_S\dot{\boldsymbol{\theta}}_S, \quad (5)$$

where $\boldsymbol{K}_S$ and $\boldsymbol{D}_S$ are the stiffness and viscosity matrices of the soft material; $\Delta\boldsymbol{\theta}_S := \boldsymbol{\theta}_{S,\mathrm{ref}} - \boldsymbol{\theta}_S$ denotes the error, and ($\boldsymbol{\theta}_{S,\mathrm{ref}}$ represents the original coordinates of the soft part without deformation). Note that $\boldsymbol{K}_S$ and $\boldsymbol{D}_S$ are constant matrices because we consider the passive viscoelasticity of the structure.

The problem in controlling the hybrid system given by (4) is how to generate the control input $\boldsymbol{\tau}_R$, which is the actuation torque in the rigid-body links, considering the effects of passive elasticity given by (5) and the total system stability. QP-based inverse dynamics is a commonly-used approach in the rigid-body multi-link system for optimizing the joint torque and contact forces to achieve an appropriate task-space control, typically given as:

$$\boldsymbol{f} = \boldsymbol{f}_{\mathrm{ref}} + \boldsymbol{K}\Delta\boldsymbol{p} + \boldsymbol{D}\Delta\boldsymbol{v} \quad (6)$$

where $\boldsymbol{f}$ and $\boldsymbol{f}_{\mathrm{ref}}$ are the task-space force and its reference value, respectively (generally, it is a 6D wrench including both linear force and torque); $\boldsymbol{K}$ and $\boldsymbol{D} \in \mathbb{R}^{m\times m}$ are the task-space stiffness and viscosity matrices; $\Delta\boldsymbol{p}$ and $\Delta\boldsymbol{v}$ are position and velocity errors. Specifically, in a humanoid robot system, the center of gravity (COG), angular momentum, foot position, or orientation are usually selected as the task space. However, we find that it would be difficult for the QP-based approach to provide a feasible solution, and discuss this problem in the next subsection.

B. Expected Problem with QP-based Control in Hybrid-link System

The procedure of the centroidal balance control approach using the *standard* QP method for humanoid robots is summarized as follows:

1) **Resolved acceleration control** calculates $\ddot{\boldsymbol{q}}_{\mathrm{cmd}}$ to achieve control input $\dot{\boldsymbol{v}}_{\mathrm{cmd}}$ in the task space;
2) **Inverse dynamics** calculates the left-hand side of the floating-base dynamics equation (4): $\boldsymbol{\Gamma}(\boldsymbol{q}, \dot{\boldsymbol{q}}, \ddot{\boldsymbol{q}}_{\mathrm{cmd}}) := \mathcal{M}(\boldsymbol{q})\ddot{\boldsymbol{q}}_{\mathrm{cmd}} + \boldsymbol{\beta}(\boldsymbol{q}, \dot{\boldsymbol{q}})$;
3) The QP tries to find a feasible control inputs solution because these are not uniquely determined in general.

If $\boldsymbol{\tau}_S$ is given by (5), the unknown control inputs in (4) are $\boldsymbol{\tau}_R$ and $\boldsymbol{f}_C$. The QP for these values is formulated by

$$\min_{\boldsymbol{\tau}_R, \boldsymbol{f}_C} \frac{1}{2}\left\|\boldsymbol{\Gamma}(\boldsymbol{q}, \dot{\boldsymbol{q}}, \ddot{\boldsymbol{q}}_{\mathrm{cmd}}) - \begin{bmatrix}\boldsymbol{0}^T & \boldsymbol{\tau}_R^T & \boldsymbol{\tau}_S^T\end{bmatrix}^T - \mathcal{J}_C^T\boldsymbol{f}_C\right\|_{\boldsymbol{W}}^2$$
$$\text{s.t.} \quad (5),\ \boldsymbol{C}_1\boldsymbol{\tau}_R \le \boldsymbol{d}_1,\ \boldsymbol{C}_2\boldsymbol{f}_C \le \boldsymbol{d}_2 \quad (7)$$

where ($\boldsymbol{C}_1$, $\boldsymbol{d}_1$) and ($\boldsymbol{C}_2$, $\boldsymbol{d}_2$) are coefficient matrices and vectors that represent the constraints on the joint torque and foot contact force (Pfaffian constraint), respectively, and $\boldsymbol{W}$ is the weighting matrix.

However, it is expected that this QP fails to find a feasible solution because of the following reason. Extracting the lower $3N_S$ rows in (4) yields

$$\mathcal{M}_S\ddot{\boldsymbol{q}} + \boldsymbol{\beta}_S = \boldsymbol{\tau}_S + \mathcal{J}_{C,S}^T \boldsymbol{f}_C \tag{8}$$

where $\mathcal{J}_{C,S}^T$ is the lower $3N_S$ block in $\mathcal{J}_C^T$. The size of $\mathcal{J}_{C,S}^T$ is $3N_S \times 3N_C$. For the double support state described in Section IV, it is 36×24 because of $N_S = 12$ and $N_C = 8$. In this case, we cannot find the solution of $\boldsymbol{f}_C$ to satisfy the equality constraint given by (5). Alternatively, it is expected that the feasible solution space is very limited. Therefore, we consider that the QP-based method is not appropriate for high soft-part DoF scenarios.

III. Compliance Optimization in Single Support

A. Compliance Control in Single Support State

Considering a single foot support state with the surface contact ideally maintained, let $\boldsymbol{\eta}_F \in \mathbb{R}^6$ denote the velocity twist vector of the contacting foot. In the single support state, $\boldsymbol{\eta}_F = \boldsymbol{0}$ holds, as shown in Fig. 2(b). From this constraint, we can represent $\boldsymbol{\eta}_0$ by the rest of $\dot{\boldsymbol{q}}$, and obtain $\dot{\boldsymbol{q}} = \boldsymbol{G}_1\dot{\boldsymbol{\theta}}$, where $\boldsymbol{G}_1$ is the Jacobian matrix mapping from $\dot{\boldsymbol{\theta}}$ to $\dot{\boldsymbol{q}}$ [10]. We can derive the dynamics of the single support state in a manner similar to the fixed-base system as follows:

$$\begin{bmatrix} \boldsymbol{M}_R & \boldsymbol{M}_{RS} \\ \boldsymbol{M}_{RS}^T & \boldsymbol{M}_S \end{bmatrix} \ddot{\boldsymbol{\theta}} + \begin{bmatrix} \boldsymbol{b}_R \\ \boldsymbol{b}_S \end{bmatrix} = \begin{bmatrix} \boldsymbol{\tau}_R \\ \boldsymbol{\tau}_S \end{bmatrix} + \boldsymbol{J}_C^T \boldsymbol{f}_C \tag{9}$$

where $\boldsymbol{M}_*(\boldsymbol{\theta})$, $\boldsymbol{b}_*(\boldsymbol{\theta}, \dot{\boldsymbol{\theta}})$ and $\boldsymbol{J}_C^T$ are counterparts of $\mathcal{M}(\boldsymbol{q})$, $\boldsymbol{\beta}(\boldsymbol{q}, \dot{\boldsymbol{q}})$ and $\mathcal{J}_C^T$, respectively. In this study, $\boldsymbol{\theta} := [\boldsymbol{\theta}_R^T\ \boldsymbol{\theta}_S^T]^T$ is the *hybrid* joint coordinate vector, and $\boldsymbol{\tau} := [\boldsymbol{\tau}_R^T\ \boldsymbol{\tau}_S^T]^T$ is the *hybrid* joint torque.

In the following sections, we assume a joint compliance control achieved by

$$\boldsymbol{\tau} = \begin{bmatrix} \boldsymbol{\tau}_{R,\mathrm{ref}} \\ \boldsymbol{0} \end{bmatrix} + \underbrace{\begin{bmatrix} \boldsymbol{K}_R & \boldsymbol{K}_{RS} \\ \boldsymbol{O} & \boldsymbol{K}_S \end{bmatrix}}_{\boldsymbol{K}_\theta} \Delta\boldsymbol{\theta} + \underbrace{\begin{bmatrix} \boldsymbol{D}_R & \boldsymbol{D}_{RS} \\ \boldsymbol{O} & \boldsymbol{D}_S \end{bmatrix}}_{\boldsymbol{D}_\theta} \Delta\dot{\boldsymbol{\theta}} \tag{10}$$

where $\boldsymbol{\tau}_{R,\mathrm{ref}}$ is a feed-forward torque, $\boldsymbol{K}_\theta$ and $\boldsymbol{D}_\theta$ are the *hybrid* joint stiffness and viscosity matrices, respectively. The hybrid joint stiffness and viscosity can be divided into two parts: $\widehat{\boldsymbol{K}}_R := \begin{bmatrix} \boldsymbol{K}_R & \boldsymbol{K}_{RS} \end{bmatrix}$ and $\widehat{\boldsymbol{D}}_R := \begin{bmatrix} \boldsymbol{D}_R & \boldsymbol{D}_{RS} \end{bmatrix}$ are the *active* stiffness and viscosity matrices, respectively; while $\boldsymbol{K}_S$ and $\boldsymbol{D}_S$ are the *passive* matrices defined in (5). Besides, note that $\boldsymbol{\theta}_{\mathrm{ref}}$ represents an equilibrium strain considering the gravity effect in this case. Because the formulation of viscosity is similar to that of stiffness, we focus exclusively on stiffness in the derivation in the following sections.

B. Static-Based Compliance Optimization (Including Static-Based Compliance Optimization for Open Kinematic Chain)

The relationship between hybrid joint-space stiffness and task-space stiffness is represented as [11]

$$\boldsymbol{J}\boldsymbol{C}_\theta\boldsymbol{J}^T = \boldsymbol{C} \tag{11}$$

where $\boldsymbol{J}$ is the Jacobian matrix of tasks, and $\boldsymbol{C}_* := \boldsymbol{K}_*^{-1}$ denotes the inverse matrix of the stiffness, i.e., compliance matrix. We can calculate $\boldsymbol{C}_\theta = \boldsymbol{K}_\theta^{-1}$ as

$$\boldsymbol{C}_\theta = \begin{bmatrix} \boldsymbol{C}_R & \boldsymbol{C}_{RS} \\ \boldsymbol{O} & \boldsymbol{C}_S \end{bmatrix} = \begin{bmatrix} \boldsymbol{K}_R^{-1} & -\boldsymbol{K}_R^{-1}\boldsymbol{K}_{RS}\boldsymbol{K}_S^{-1} \\ \boldsymbol{O} & \boldsymbol{K}_S^{-1} \end{bmatrix}. \tag{12}$$

We can find that $\boldsymbol{C}_\theta$ is upper-triangle block matrix as well as $\boldsymbol{K}_\theta$. Corresponding to the block matrices in $\boldsymbol{C}_\theta$, we can divide $\boldsymbol{J}$ into two blocks $\boldsymbol{J}_R$ and $\boldsymbol{J}_S$: $\boldsymbol{J} = [\boldsymbol{J}_R\ \boldsymbol{J}_S]$, representing the rigid and soft parts, respectively. Then, we can rewrite (11) as:

$$\begin{aligned} &\begin{bmatrix} \boldsymbol{J}_R & \boldsymbol{J}_S \end{bmatrix} \begin{bmatrix} \boldsymbol{C}_R & \boldsymbol{C}_{RS} \\ \boldsymbol{O} & \boldsymbol{C}_S \end{bmatrix} \begin{bmatrix} \boldsymbol{J}_R^T \\ \boldsymbol{J}_S^T \end{bmatrix} \\ &= \boldsymbol{J}_R \begin{bmatrix} \boldsymbol{C}_R & \boldsymbol{C}_{RS} \end{bmatrix} \begin{bmatrix} \boldsymbol{J}_R^T \\ \boldsymbol{J}_S^T \end{bmatrix} + \boldsymbol{J}_S\boldsymbol{C}_S\boldsymbol{J}_S^T = \boldsymbol{C}. \end{aligned} \tag{13}$$

The control problem is to calculate the appropriate $\boldsymbol{C}_R$ and $\boldsymbol{C}_{RS}$ when $\boldsymbol{C}$ and $\boldsymbol{C}_S$ are given. Therefore, we solve the following matrix equation for the unknown $\boldsymbol{C}_R$ and $\boldsymbol{C}_{RS}$:

$$\boldsymbol{J}_R\widehat{\boldsymbol{C}}_R\boldsymbol{J}^T = \widehat{\boldsymbol{C}} := \boldsymbol{C} - \boldsymbol{J}_S\boldsymbol{C}_S\boldsymbol{J}_S^T \tag{14}$$

where $\widehat{\boldsymbol{C}}_R := \begin{bmatrix} \boldsymbol{C}_R & \boldsymbol{C}_{RS} \end{bmatrix}$. In the following sections, $\widehat{\boldsymbol{C}}_R$ and $\boldsymbol{C}_S$ are referred to as the active compliance and the passive compliance, respectively. When there are redundant DOFs, the solution of $\widehat{\boldsymbol{C}}_R$ is not uniquely determined. Instead, we solve the following optimization problem for $\widehat{\boldsymbol{C}}_R$:

$$\min_{\widehat{\boldsymbol{C}}_R} \frac{1}{2}\|\widehat{\boldsymbol{C}}_{R,\mathrm{ref}} - \widehat{\boldsymbol{C}}_R\|^2 \quad \text{s.t. (14).} \tag{15}$$

where $\widehat{\boldsymbol{C}}_{R,\mathrm{ref}}$ is the reference (or null-space) active compliance usually set as $\widehat{\boldsymbol{C}}_{R,\mathrm{ref}} = [\frac{1}{y}\boldsymbol{E}\ \boldsymbol{O}]$ (y is a positive constant). The closed-form solution of this optimization problem is according to (2).

IV. Compliance Optimization in Double Support

A. Static-based Compliance Optimization in Double Support

The situation shown in Fig. 2(c), where the robot makes contact with the environment via two links, corresponds to the double-support state of a bipedal robot with a closed kinematic chain involved in the system. We can define the closed kinematic chain as a reduced space, and make a mapping between the closed-chain space and joint space using $\dot{\boldsymbol{\theta}} = \boldsymbol{G}_2\dot{\boldsymbol{\theta}}_2$, where $\dot{\boldsymbol{\theta}}_2$ is the velocity of the closed-chain space, and $\boldsymbol{G}_2$ represents the mapping matrix. Using $\boldsymbol{G}_2$, we can obtain the Jacobian matrix between the task-space velocity $\boldsymbol{v}$ and $\dot{\boldsymbol{\theta}}_2$ as

$$\boldsymbol{v} = \boldsymbol{J}_2\dot{\boldsymbol{\theta}}_2, \quad \boldsymbol{J}_2 := \boldsymbol{J}\boldsymbol{G}_2. \tag{16}$$

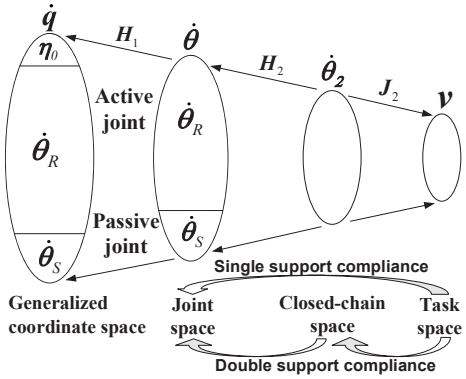

Fig. 3. Relationship between the different spaces of a hybrid system comprising a closed kinematic chain. The ovals in the figure represent the velocity spaces. The solid straight arrows show the transformation direction between different velocities. The hollow curved arrows represent the transformation relationship between different space compliance. In the single-support case, the task-space compliance can be directly transformed into joint space; while in the double-support case, a closed-chain space is required.

Fig. 3 illustrates the relationship between $\dot{\boldsymbol{q}}$, $\dot{\boldsymbol{\theta}}$, $\dot{\boldsymbol{\theta}}_2$, and $\boldsymbol{v}$. The constraints of the single and double support reduce the order of the generalized velocity from $\dot{\boldsymbol{q}}$ to $\dot{\boldsymbol{\theta}}$ and $\dot{\boldsymbol{\theta}}_2$, respectively.

The stiffness relationship is represented as follows [10]:

$$\boldsymbol{J}_2\boldsymbol{C}_2\boldsymbol{J}_2^T = \boldsymbol{C}, \tag{17}$$

$$\boldsymbol{G}_2^T\boldsymbol{K}_\theta\boldsymbol{G}_2 = \boldsymbol{K}_2 \tag{18}$$

where $\boldsymbol{C}_2 = \boldsymbol{K}_2^{-1}$ is the compliance in the closed-chain space. To obtain the hybrid stiffness $\boldsymbol{K}_\theta$, we firstly solve $\boldsymbol{C}_2$ according to (17) by

$$\min_{\boldsymbol{C}_2} \ \frac{1}{2}\|\boldsymbol{C}_{2,\mathrm{ref}} - \boldsymbol{C}_2\|^2 \quad \text{s.t. (17)} \tag{19}$$

where

$$\boldsymbol{C}_{2,\mathrm{ref}} = \boldsymbol{K}_{2,\mathrm{ref}}^{-1} = \left(\boldsymbol{G}_2^T\begin{bmatrix} y\boldsymbol{E} & \boldsymbol{O} \\ \boldsymbol{O} & \boldsymbol{K}_S \end{bmatrix}\boldsymbol{G}_2\right)^{-1} \tag{20}$$

is the reference stiffness in the closed-chain space. The general solution is according to (2).

Then, we calculate $\boldsymbol{K}_2 = \boldsymbol{C}_2^{-1}$ and solve (18) for the given stiffness $\boldsymbol{K}_S$. Similar to Section III-B, we divide $\boldsymbol{G}_2$ into two blocks $\boldsymbol{G}_{2R}$ and $\boldsymbol{G}_{2S}$: $\boldsymbol{G}_2 = [\boldsymbol{G}_{2R}^T \ \boldsymbol{G}_{2S}^T]^T$ and rewrite (18) as follows:

$$\boldsymbol{G}_{2R}^T\widehat{\boldsymbol{K}}_R\boldsymbol{G}_2 = \widehat{\boldsymbol{K}}_2 := \boldsymbol{K}_2 - \boldsymbol{G}_{2S}^T\boldsymbol{K}_S\boldsymbol{G}_{2S}. \tag{21}$$

Considering the reference stiffness $\widehat{\boldsymbol{K}}_{R,\mathrm{ref}} = \begin{bmatrix} y\boldsymbol{E} & \boldsymbol{O} \end{bmatrix}$, the optimization problem can be expressed by

$$\min_{\widehat{\boldsymbol{K}}_R} \ \frac{1}{2}\|\widehat{\boldsymbol{K}}_{R,\mathrm{ref}} - \widehat{\boldsymbol{K}}_R\|^2 \quad \text{s.t. (21)} \tag{22}$$

and the general solution of this problem is in the same form of (2).

B. Dynamically-consistent Optimization

In the previous subsection, we calculated the active compliance based on the *static* compliance relationship (17). In this subsection, we propose a *dynamically-consistent* optimization for hybrid compliance control, focusing on the double support state. Although the obtained $\boldsymbol{C}_2$ for the given task-space $\boldsymbol{C}$ will be equivalent to the operational-space control (OSC) [12], we begin the discussion on the dynamically-consistent optimization in a standard case before extending it to the specific hybrid situation.

For the $\dot{\boldsymbol{\theta}}_2$ space, the dynamically-consistent compliance formulation [9] is represented as follows:

$$\boldsymbol{J}_2\boldsymbol{C}_2 = \boldsymbol{C}\boldsymbol{J}_2^{T\dagger} \tag{23}$$

where $\boldsymbol{X}^\dagger$ denotes the *dynamically-consistent inverse* [12] of a matrix $\boldsymbol{X}$, defined with the inertia matrix $\boldsymbol{M}$ as:

$$\boldsymbol{X}^\dagger := \boldsymbol{M}^{-1}\boldsymbol{X}^T(\boldsymbol{X}\boldsymbol{M}^{-1}\boldsymbol{X}^T)^{-1}. \tag{24}$$

Equation (23) is equivalent to

$$\boldsymbol{K}\boldsymbol{J}_2 = \boldsymbol{J}_2^{T\dagger}\boldsymbol{K}_2, \tag{25}$$

In (23) and (25), the general solution is obtained with the null-space stiffness $\boldsymbol{Y}$. However, there is no guarantee that the obtained solution is positive-definite, which should be satisfied as a necessary stability condition. In [9], a closed-form solution guarantees the positive-definiteness based on (23).

In this study, we consider a special case where $\boldsymbol{Y}$ is multiplied by the inertia as $\boldsymbol{Y} = y\boldsymbol{M}$. However, it was reported [13] that this class of null-space compliance degrades the control performance for inertial parameter errors.

The general solution of (25) is given as:

$$\boldsymbol{K}_2 = \boldsymbol{J}_2^T\boldsymbol{K}\boldsymbol{J}_2 + (\boldsymbol{E} - \boldsymbol{J}_2^T\boldsymbol{J}_2^{T\dagger})\boldsymbol{Y} \tag{26}$$

because $(\boldsymbol{X}^{T\dagger})^\sharp = \boldsymbol{X}^T$ is satisfied.

Then, we derive the stiffness matrix that is equivalent to the operational-space control. If we consider a joint torque $\boldsymbol{\tau}_2 = \boldsymbol{K}_2\Delta\boldsymbol{\theta}_2$ (as mentioned above, we focus only on stiffness), we obtain

$$\boldsymbol{\tau}_2 = \boldsymbol{J}_2^T\boldsymbol{f} + (\boldsymbol{E} - \boldsymbol{J}_2^T\boldsymbol{J}_2^{T\dagger})\boldsymbol{y} \tag{27}$$

where $\boldsymbol{f} := \boldsymbol{K}\boldsymbol{J}\Delta\boldsymbol{\theta}_2$ and $\boldsymbol{y} := \boldsymbol{Y}\Delta\boldsymbol{\theta}_2$ are the control inputs in the task-space and the reduced space of $\boldsymbol{\theta}_2$, respectively. Equation (27) represents the operational-space control.

Substituting $\boldsymbol{Y} = y\boldsymbol{M}$ into (26) yields

$$\boldsymbol{K}_2 = \boldsymbol{J}_2^T\boldsymbol{K}\boldsymbol{J}_2 + y(\boldsymbol{M} - \boldsymbol{J}_2^T\boldsymbol{\Lambda}\boldsymbol{J}_2), \tag{28}$$

where $\boldsymbol{\Lambda} := (\boldsymbol{J}_2\boldsymbol{M}^{-1}\boldsymbol{J}_2^T)^{-1}$. We found that the solution in (28) is a special case of (26). Moreover, we can prove that (28) is always positive definite, using the singular value decomposition of the Jacobian matrix.

However, the passive stiffness $\boldsymbol{K}_S$ is given in the hybrid system. Thus, we have to consider this constraint in the null-space stiffness setting. Specifically, we set the null-space stiffness in (26) as

$$\boldsymbol{Y} = \boldsymbol{G}_2^T\begin{bmatrix} y\boldsymbol{M}_R & \boldsymbol{O} \\ \boldsymbol{O} & \boldsymbol{K}_S \end{bmatrix}\boldsymbol{G}_2. \tag{29}$$

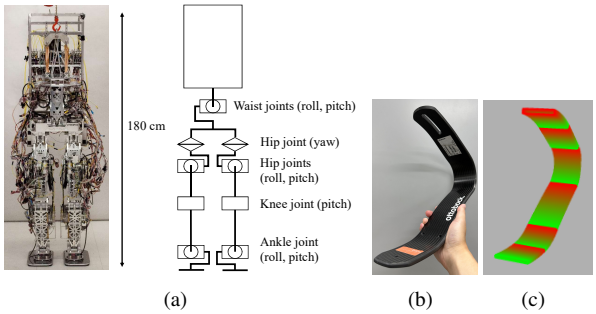

(a) (b) (c)

Fig. 4. (a) Configuration of rigid Hydra. (b) a sports prosthesis leg. (c) PCS model of sports prosthesis for simulation. The model in (c) is divided into six segments. Each segment is represented by a gradient color ranging from red to green.

TABLE I

PARAMETER SETTINGS IN SIMULATIONS

(y and z are the null-space stiffness and damping values, respectively)

(a) Single- & double-support balance control

	COG gain α_i	y	z
PD	/	100	1.0
static-based	1.0, 1.0, 1000	100	1.0
dynamically-consistent	1.0, 1.0, 1000	100	$2\sqrt{y}$

(b) Vertical hopping control (dynamically-consistent)

	COG gain α_i	y	z
Take-off phase	1.0, 1.0, 1000	300	0.2*$2\sqrt{y}$
Flight phase (PD)	/	500	5.0
Touch-down phase	1.0, 1.0, 1000	100	$2\sqrt{y}$

Finally, after calculating $\boldsymbol{K}_2$ by (26), we can obtain the active stiffness $\widehat{\boldsymbol{K}}_R$ by solving (22) similarly to the previous subsection. While in the dynamically-consistent case, we have $\widehat{\boldsymbol{K}}_{R,\mathrm{ref}} = \begin{bmatrix} y\boldsymbol{M}_R & \boldsymbol{O} \end{bmatrix}$.

V. SIMULATIONS

A. Simulation Setting

We validate the proposed methods using forward dynamics simulations, assuming a rigid-soft hybrid robot comprising of a hydrostatically-driven humanoid robot Hydra (180 cm, 74 kg, 14 DOFs, as shown in Fig. 4(a)) [14] as a rigid part, and two sports prostheses (Runner 1E91, Ottobock, as shown in Fig. 4(b)) connected to its feet as soft parts represented by the PCS model (as shown in Fig. 4(c)). In this study, each prosthesis is divided into 6 segments, each segment with 3 angular strain DOFs. Therefore, the whole hybrid system has 56 DOFs (floating base: 6, rigid part: 14, soft part: $3N_S = 3 \times 6 \times 2 = 36$).

We simulated three scenarios: 1) single-support balancing (the posture is shown in Fig. 5(a)), 2) double-support balancing (as shown in Fig. 6(a)), and 3) vertical hopping. We set the stiffness and damping matrices of each PCS model as $\boldsymbol{K}_S = 50\boldsymbol{E}$ and $\boldsymbol{D}_S = 0.02\boldsymbol{E}$, respectively. The general control framework of the proposed method is illustrated in Fig. 7. In the proposed approach, the matrices $\boldsymbol{K}$ and $\boldsymbol{D}$ of the COG task are determined based on the capture point feedback control of the COG-ZMP model and equivalent COG viscoelasticity [15] as follows:

$$\boldsymbol{K} = m\omega^2(\mathrm{diag}\{\alpha_i\} - \boldsymbol{E}),\ \boldsymbol{D} = m\omega\ \mathrm{diag}\{\alpha_i\} \qquad (30)$$

where m is the total mass; ω is a constant; $\alpha_i > 1$ is the feedback gain parameter. This literature [15] reported that the capture point feedback maximizes the stability region under the ZMP constraints. In the static standing, the desired COG is a fixed point. In this study, we set the feed-forward torque $\boldsymbol{\tau}_{R,\mathrm{ref}}$ as the gravity compensation term. The value of the null-space viscoelasticity is determined by trial and error. Table I(a) summarizes the parameters used in the simulations. The simulation process is shown in `Accompanying video`.

B. Single-support balance control

In this subsection, we compare static compliance optimization and simple PD control (with constant joint PD) in the single-support standing. In this scenario, we added an external disturbance (100 N within 0.02 s) to the body link in the $+x$ direction at 1 s. Fig. 5 depicts the simulation results of the (b) COG and (c) ZMP. In each graph, the blue and black lines indicate the proposed static-based compliance and PD control results. In the PD control case, the COG and ZMP diverged after the external disturbance, and the robot fell down eventually. However, in the proposed method, the standing balance was maintained, although small oscillations of the COG and ZMP remained. We also compared the proposed method in other scenarios, such as adding a $+y$ disturbance on the body.

C. Double-support balance control

In the scenario shown in Fig. 6(a), we added an external disturbance (1,000 N within 0.02 s) to the body link in the x direction. Fig. 6(b) and (c) depict the simulation results, where blue, magenta, and green lines indicate the results of the static-based optimization, dynamically-consistent optimization, respectively. In the case of the static-based method, the COG and ZMP diverged after the external disturbance, and the robot fell down after approximately 3 s. For the dynamically consistent method, however, the standing balance was maintained without falling down. In summary, this result validates that the dynamically consistent method optimizes the active compliance considering the variable inertial effect as opposed to constant null-space viscoelasticity in the static-based case. Moreover, we also compared the proposed method in the case of a $+y$ disturbance added to the body.

D. Vertical hopping and landing motion control

Finally, we demonstrate a vertical hopping motion using the proposed dynamically-consistent method. In this motion, the desired COG has a continuous trajectory. The hopping motion consists of three phases: take-off (including squat motion), flight, and landing phases. We design a reference trajectory of the COG using the 3D ZMP model [16], assuming the double support state in the take-off and landing phases. Table I(b) summarizes the setting of the parameters.

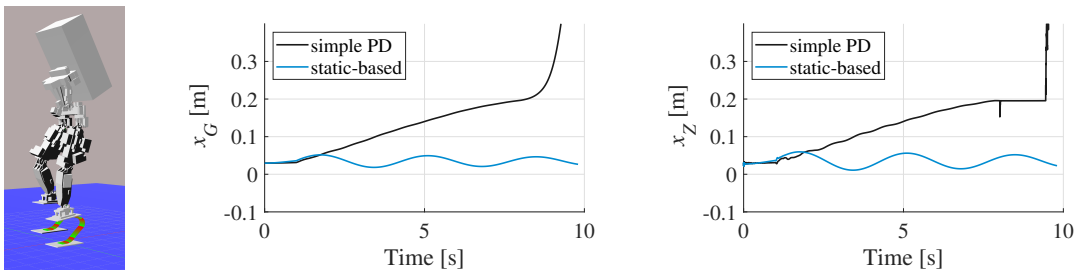

(a) (b) COG in the x-axis (c) ZMP in the x-axis

Fig. 5. (a) Single-support hybrid Hydra in simulation. (b) and (c) are simulation results of single support balancing. An external impact (100 N $\times$ 0.02 s) was added to the body link in $+x$ direction at 1 s.

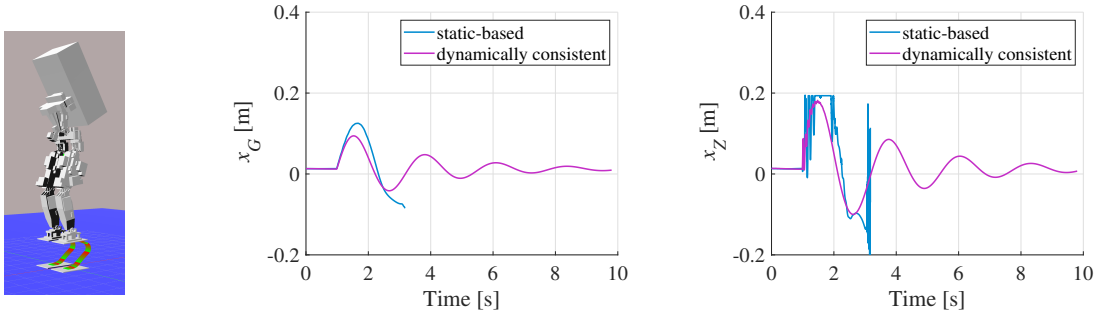

(a) (b) COG in the x-axis (c) ZMP in the x-axis

Fig. 6. (a) Double-support hybrid Hydra in simulation. (b) and (c) are simulation results of double support balancing. An external impact (1,000 N $\times$ 0.02 s) was added to the body link in the $+x$ direction at 1 s.

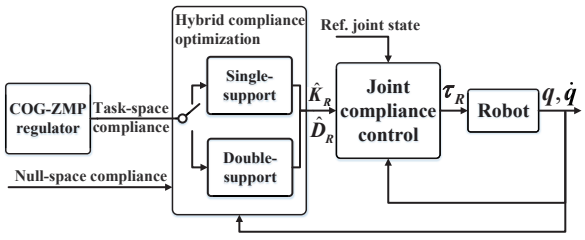

Fig. 7. General control framework of our proposed method.

In the current implementation, we applied the reference trajectory of the hybrid joint coordinate $\boldsymbol{\theta}_{\mathrm{ref}}$ solving by inverse kinematics. In a preliminary simulation, we found unstable motions during hopping, which we attributed to the calculation of $\boldsymbol{\theta}_{S,\mathrm{ref}}$, fed back to $\boldsymbol{\tau}_R$ by the non-diagonal block $\boldsymbol{K}_{RS}$ in $\boldsymbol{K}_\theta$. Therefore, we set $\boldsymbol{K}_{RS} = \boldsymbol{O}$ when solving (21) in the take-off phase. Eventually, we can rewrite (21) as follows:

$$\boldsymbol{G}_{2R}^T \boldsymbol{K}_R \boldsymbol{G}_{2R} = \widehat{\boldsymbol{K}}_2. \tag{31}$$

Fig. 8 shows snapshots of a single hopping motion obtained during the simulation. Fig. 9 illustrates the COG trajectories in the z-axis. In the reference trajectory, indicated by the black solid line, the duration of the flight phase was 0.15 s (between two vertical dashed lines in Fig. 9), and the jumping height was about 0.03 m. In the simulation result, the duration of the flight phase, indicated by the magenta line, was about 0.3 s (the gray region in Fig. 9), and the jumping height was 0.09 m at 0.68 s, which was three times higher than that in the reference. We observed that the simulated trajectory of the COG lagged behind the reference trajectory. Such a higher jump was obtained because elastic energy was stored in the prosthesis during the take-off phase and used for acceleration.

For comparison, we also simulated a hopping motion using the original Hydra model (without any soft parts) for the same jumping height and duration. Fig. 10 shows the waist, hip, knee, and ankle joint torques during the hopping motion, where the black solid and dashed lines indicate the results using the hybrid Hydra and original models, respectively. In the take-off phase, it is observed that the peak values of the waist, hip, and ankle torques of the hybrid Hydra were smaller than those of the original model. For example, the peak torque of the waist joint was about 60 Nm at 0.01 s in the hybrid Hydra while it was about 277 Nm at 0.5s in the original model.

VI. Conclusion

This study presented a control framework for a rigid-soft hybrid robot system in which the deformation was represented using the PCS model. The obtained results are summarized as follows:

1) We proposed the compliance optimization framework for a hybrid-link system in two states: single and double support. The proposed *static* compliance control optimized the active compliance matrix including the coupling term between the active and passive joints. We further proposed

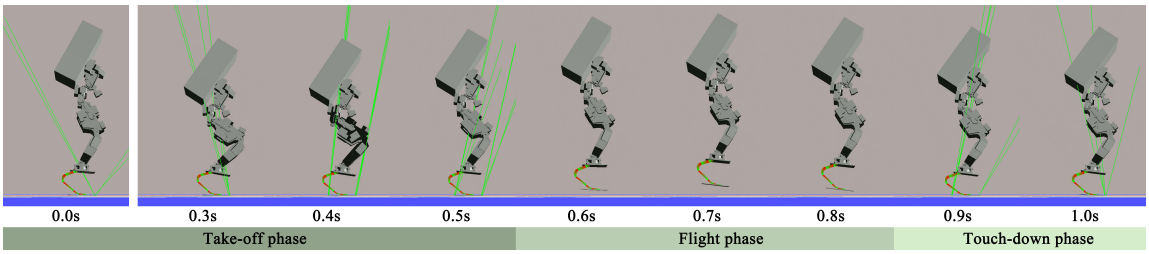

Fig. 8. Snapshots of dynamically-consistent optimization simulation during vertical hopping and landing (one period). The green line shows the ground reaction force on each vertex of the contact plane.

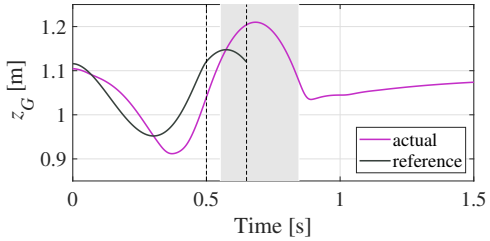

Fig. 9. COG position in the z-axis of vertical hopping and landing motion on hybrid Hydra. The black line is the reference trajectory generated by the 3D ZMP model (only until the touch-down moment); the magenta line is the control result of the simulation. The dashed lines represent the take-off and touch-down moment in the reference. The gray region shows the flight phase of the simulation. The relative jumping height in the simulation is 0.09m (relative to the take-off position).

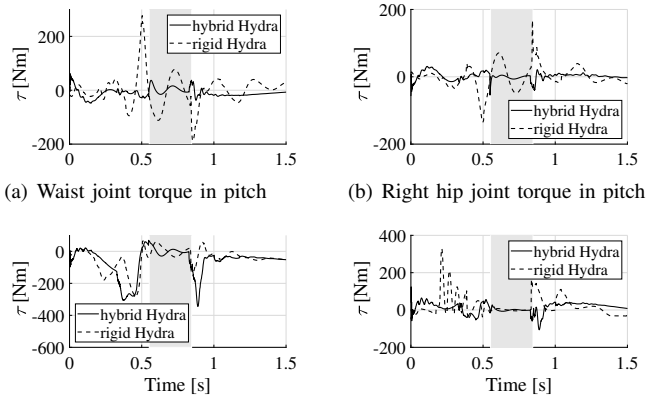

(a) Waist joint torque in pitch
(b) Right hip joint torque in pitch
(c) Right knee joint torque
(d) Right ankle joint torque in pitch

Fig. 10. Joint torques in the vertical hopping and landing motion. The torque of the left-side joints is similar to that of the right-side joints. The gray region shows the flight phase.

the dynamically consistent compliance optimization for the double support state.

2) We validated the proposed methods through forward dynamic simulation, assuming a hybrid-link system comprised of a humanoid robot and sports prosthesis. In the single-support, the proposed static compliance method stabilized the upright posture against an external disturbance while it fell down with PD control. In the double-support, the dynamically consistent optimization method exhibited more robust and stable balancing for an external disturbance that was 10 times larger than that in the single-support case.

3) We applied the dynamically consistent optimization method to a vertical hopping motion. The proposed method achieved 3 times higher jumping height than the reference trajectory. We consider that the passive elasticity in the hybrid link system contributed to storing the elastic energy in the take-off phase and utilizing it for higher jumping.

References

[1] R. Niiyama, S. Nishikawa, and Y. Kuniyoshi, "Athlete robot with applied human muscle activation patterns for bipedal running," in *Proc. of IEEE-RAS Intl. Conf. on Humanoid Robotics, 2010*, pp. 498–503.

[2] C. G. Rose and M. K. O'Malley, "Hybrid rigid-soft hand exoskeleton to assist functional dexterity," *IEEE Robotics and Automation Letters*, vol. 4, no. 1, pp. 73–80, 2018.

[3] S. S. Antman, *Nonlinear Problems of Elasticity*, 2005, vol. 107.

[4] F. Renda, F. Boyer, J. Dias, and L. Seneviratne, "Discrete cosserat approach for multisection soft manipulator dynamics," *IEEE Transactions on Robotics*, vol. 34, no. 6, pp. 1518–1533.

[5] T. Ishigaki and K. Yamamoto, "Dynamics computation of a hybrid multi-link humanoid robot integrating rigid and soft bodies," in *Proc. of IEEE-RSJ IROS*, 2021, pp. 2793–2798.

[6] C. M. Best, M. T. Gillespie, P. Hyatt, L. Rupert, V. Sherrod, and M. D. Killpack, "A new soft robot control method: Using model predictive control for a pneumatically actuated humanoid," *IEEE Robotics & Automation Magazine*, vol. 23, no. 3, pp. 75–84, 2016.

[7] M. Manti, V. Cacucciolo, and M. Cianchetti, "Stiffening in soft robotics: A review of the state of the art," *IEEE Robotics & Automation Magazine*, vol. 23, no. 3, pp. 93–106, 2016.

[8] L. Weerakoon and N. Chopra, "Passivity-based task space control of hybrid rigid-soft (hyriso) robots with parametric uncertainty," in *2022 IEEE CDC*, pp. 771–776.

[9] K. Yamamoto, T. Ishigaki, and Y. Nakamura, "Humanoid motion control by compliance optimization explicitly considering its positive definiteness," *IEEE Transactions on Robotics*, 2021.

[10] K. Yamamoto, "Robust Walking by Resolved Viscoelasticity Control Explicitly Considering Structure-Variability of a Humanoid," in *Proc. of IEEE ICRA*, 2017, pp. 3461–3468.

[11] R. P. Paul, "Compliance and control," in *Proc. of the 1976 Joint Automatic Control Conference*, 1976, pp. 694–699.

[12] O. Khatib, "A Unified Approach for Motion and Force Control: The Operational Space Formulation," *IEEE International Journal of Robotics and Automation*, vol. 3, no. 1, pp. 43–53, 1987.

[13] J. Nakanishi and et al., "Operational space control: A theoretical and empirical comparison," *The International Journal of Robotics Research*, vol. 27, no. 6, pp. 737–757, 2008.

[14] T. Ko, K. Murotani, K. Yamamoto, and Y. Nakamura, "Whole-body compliant motion by sensor integration of an eha-driven humanoid hydra," *International Journal of Humanoid Robotics*, 2021.

[15] K. Yamamoto, "Resolved multiple viscoelasticity control for a humanoid," *IEEE Robotics and Automation Letters*, vol. 3, no. 1, pp. 44–51, 2017.

[16] T. Sugihara, K. Imanishi, T. Yamamoto, and S. Caron, "3d biped locomotion control including seamless transition between walking and running via 3d zmp manipulation," in *Proc. of IEEE-RAS ICRA, 2021*, pp. 6258–6263.